chemistry

MDPI

Article

Unveiling the Unexpected Reactivity of Electrophilic Diazoalkanes in [3+2] Cycloaddition Reactions within Molecular Electron Density Theory

Luis R. Domingo [1,*], Mar Ríos-Gutiérrez [1] and Nivedita Acharjee [2]

[1] Department of Organic Chemistry, University of Valencia, Dr. Moliner 50, Burjassot, 46100 Valencia, Spain; rios@utopia.uv.es
[2] Department of Chemistry, Durgapur Government College, J. N. Avenue, Durgapur, West Bengal 713214, India; nivchem@gmail.com
* Correspondence: domingo@utopia.uv.es

Abstract: The [3+2] cycloaddition (32CA) reactions of strongly nucleophilic norbornadiene (NBD), with simplest diazoalkane (DAA) and three DAAs of increased electrophilicity, have been studied within the Molecular Electron Density Theory (MEDT) at the MPWB1K/6-311G (d,p) computational level. These *pmr-type* 32CA reactions follow an asynchronous one-step mechanism with activation enthalpies ranging from 17.7 to 27.9 kcal·mol^{-1} in acetonitrile. The high exergonic character of these reactions makes them irreversible. The presence of electron-withdrawing (EW) substituents in the DAA increases the activation enthalpies, in complete agreement with the experimental slowing-down of the reactions, but contrary to the Conceptual DFT prediction. Despite the nucleophilic and electrophilic character of the reagents, the global electron density transfer at the TSs indicates rather non-polar 32CA reactions. The present MEDT study establishes the depopulation of the N–N–C core in this series of DAAs with the increase of the EW character of the substituents present at the carbon center is responsible for the experimentally found deceleration.

Keywords: molecular electron density theory; norbornadiene; diazoalkanes; conceptual DFT; electron localization function

Citation: Domingo, L.R.; Ríos-Gutiérrez, M.; Acharjee, N. Unveiling the Unexpected Reactivity of Electrophilic Diazoalkanes in [3+2] Cycloaddition Reactions within Molecular Electron Density Theory. *Chemistry* **2021**, *3*, 74–93. https://doi.org/10.3390/chemistry3010006

Received: 14 December 2020
Accepted: 7 January 2021
Published: 10 January 2021

1. Introduction

Norbornadiene (NBD) (bicyclo [2.2.1] hepta-2,5-diene), norbornene (bicyclo [2.2.1] hept-2-ene) and related compounds serve as key intermediates in natural product synthesis [1–3] and polymer chemistry [1,4] owing to their angularly strained unusual geometry and high reactivity. Recently, NBD has also found applications in molecular photoswitches to absorb solar radiation [5], and by 2018, more than 30 thousand publications and patents had reported their production and applications in various fields [1]. The behavior of NBD derivatives in the Wagner–Meerwein rearrangement [6,7], photochemical di-π methane rearrangement [8], Diels Alder reactions [9], catalytic reactions with alkynes [10] and several other instances [1] have established their uniqueness as organic reagents and fostered their wide synthetic applications in [3+2] cycloaddition (32CA) reactions to form isoxazolidines, triazoles, carbocycles and other heterocycles of biological and environmental relevance [11–15]. In 2001, Tam and coworkers [16,17] reported the highly regio- and stereoselective intramolecular 32CA reactions of NBD-tethered nitrones and nitrile oxides (Scheme 1).

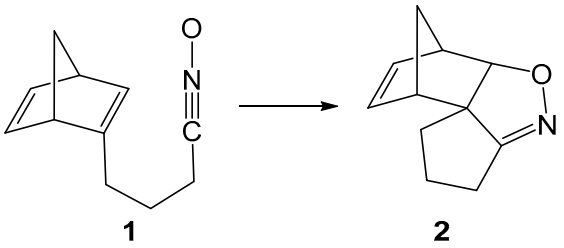

Scheme 1. Intramolecular 32CA reaction of norbornadiene (NBD)-tethered nitrile oxide **1**.

The 32CA reactions of 7-oxanorbornadiene with nitrile oxides were theoretically studied by Tajabadi et al. [18] in 2015, concluding their *anti* and *exo*-stereoselective one-step mechanism. In 2017, Domingo et al. [19] reported the complete *syn* facial stereoselectivity in the 32CA reactions of acetonitrile oxide and 7-oxanorborn-5-en-2-ones as an outcome of the unfavorable steric interactions along the *anti* approach (see Scheme 2).

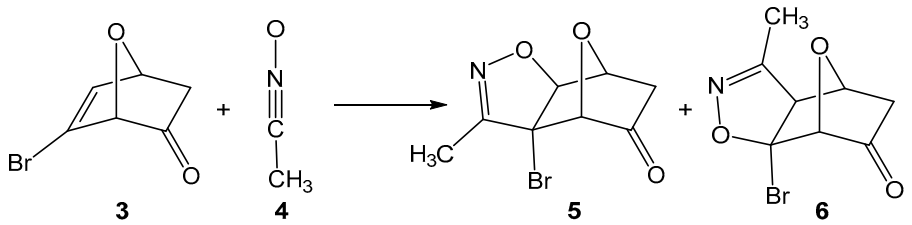

Scheme 2. 32CA reaction of 7-oxanorborn-5-en-2-one **3** with acetonitrile oxide **4**.

Very recently, two different studies [20,21] have addressed the regio-, stereo-, and enantioselectivities of the 32CA reactions of 7-isopropylidenenorbornadiene and oxonorbornadiene with nitrones, azides, and nitrileimines.

The substituent effects on the rates of the 32CA reactions between NBD and diazoalkanes (DAAs) were experimentally evidenced by Huisgen in 1963 to establish the accountability of the one-step mechanism for 32CA reactions. [22] Considering the 32CA reactions of substituted DAAs **7**–**10** with NBD **11**, (Scheme 3) Huisgen compared the one-step mechanism (Path I, Scheme 3) and the two-step addition (Path II, Scheme 3) possibilities in 32CA reactions [22].

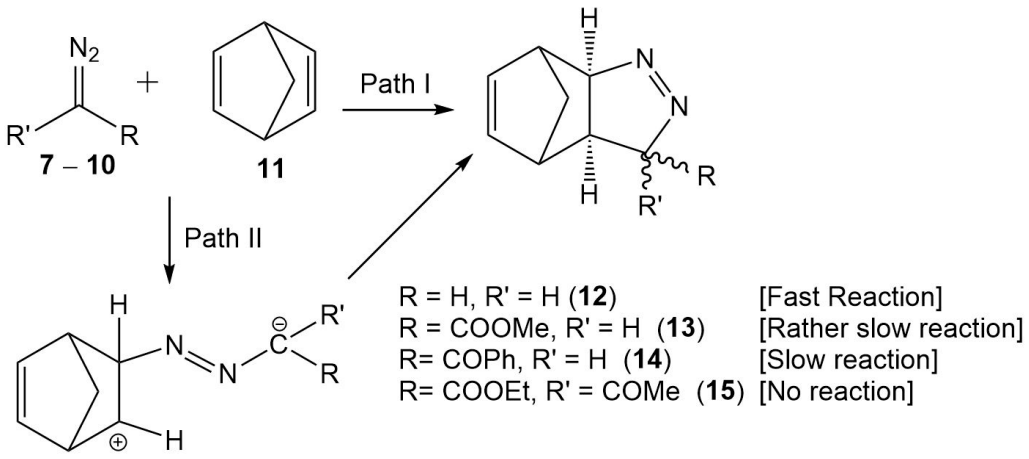

Scheme 3. 32CA reactions of substituted diazoalkanes (DAAs) **7**–**10** with NBD **11.**

The addition tendency of simplest DAA **7** with NBD **11** was maximum along this series, while the 32CA reaction slowed down by introducing electron-withdrawing (EW) carbonyl substituents at the carbon of the DAA in **8** and **9**, and finally, DAA **10**, with two carbonyl substituents, was completely inactive. Since the nucleophilic additions of NBD to the

terminal nitrogen of DAAs are well known [23], it was expected that DAAs act as an electrophilic species and NBD **11**, with two electron rich C–C double bonds, as the nucleophilic one. Hence, EW substituents in DAA should enhance the addition tendency. However, this behavior was contrary to the experimental observation (Scheme 3), and consequently, it demands a detailed explanation for the bond formation process and a rationalization of the decrease in reaction rate experimentally observed.

The underlying theory adopted for explaining 32CA reactions was based on the Frontier Molecular Orbital [24] (FMO) concept for the last 50 years, until in 2016, Domingo proposed the Molecular Electron Density Theory [25,26] (MEDT) to recognize the decisive role of the changes in electron density on the molecular reactivity. The MEDT concept, which rejects any analysis based on molecular orbitals, has explained the experimental outcome of 32CA reactions, for example, the strain promotion [27,28], selectivities [29,30], substituent effects [31–33], catalysis [34,35], etc.

Within the MEDT framework, the three-atom-components (TACs) participating in 32CA reactions are classified into four types [36], which answers their reactivity in 32CA reactions. TACs with two *pseudoradical* centers participate in *pdr-type* 32CA reactions [37], which take place very easily. TACs with one *pseudoradical* center participate in *pmr-type* 32CA reactions [38], while TACs with a carbenoid center participate in *cb-type* 32CA reactions [39]. TACs showing the absence of *pseudoradical* or carbenoid centers are classified as the zwitterionic type and participate in *zw-type* 32CA reactions [29] associated with high energy barrier demanding overcome through appropriate electrophilic-nucleophilic activations [29]. Recent studies devoted to the participation of DAAs in 32CA reactions have evidenced that DAAs have a *pseudoradical* structure, thus participating in *pmr-type* 32CA reactions [28,40].

Herein, an MEDT study for the 32CA reactions of substituted DAAs **7**–**10** with NBD **11**, experimentally studied by Huisgen [22] (Scheme 3), is performed at the MPWB1K/6-311G (d,p) computational level to explain the unexpected reactivity of these electrophilic DAAs. This MEDT report is shaped into eight sections: (i) In Section 3.1, a topological analysis of the electron localization function (ELF) [41,42] at the ground state electronic structures of the reagents is performed to structurally classify the DAAs and determine their reactivity; (ii) in Section 3.2, the global reactivity indices defined within the conceptual density functional theory [43,44] (CDFT) are discussed; (iii) in Section 3.3, the energy profiles of the feasible reaction paths and some of the properties of the corresponding stationary points are analyzed; (iv) in Section 3.4, a topological analysis of non-covalent interactions is performed to understand the origin of the stereoselectivity; (v) in Section 3.5, the molecular mechanisms of the 32CA reactions of DAAs **7** and **10** with NBD **11** are analyzed through a bonding evolution theory (BET) [45] study of the most favorable reaction paths; (vi) in Section 3.6, the topology of the ELF at the TSs is analyzed; (vii) in Section 3.7, the nature of bonding at the interatomic bonding regions is assessed through the Quantum Theory of Atoms in Molecules [46,47] (QTAIM) parameters proposed by Bader and coworkers; and finally, (viii) in Section 3.8, the origin of the deceleration with the EW substitution is analyzed.

2. Computational Methods

Optimization of the reactants, TSs, and products was done using Berny analytical gradient optimization method [48] at MPWB1K [49]/6-311G (d,p) [50]. This computational level has been recently used in studying 32CA reactions [27,28,30–32]. Frequency calculations were performed at the located stationary points to ensure that the TSs have one and only one imaginary frequency and all positive frequencies exist for the local minimum. The intrinsic reaction coordinate [51] (IRC) calculations using González-Schlegel integration method [52,53] verified the minimum energy reaction pathway connecting the reactants and the products. Solvent effects were studied by modeling the solvent acetonitrile using the polarizable continuum model [54,55] (PCM) with the self-consistent reaction field [56–58] method, and the stationary points were optimized at MPWB1K (PCM)/6-

311G (d,p) level of theory. The thermodynamic parameters, i.e., the enthalpies, entropies, and Gibbs free energies, were calculated at 298.15 K and 1 atm in acetonitrile using the standard statistical thermodynamics [50].

Equations reviewed in reference 44 are used to calculate the CDFT indices, while the global electron density transfer [59] (GEDT) at the TSs was computed from the summation of charges at each fragment derived from natural population analysis [60,61] using the equation GEDT (f) = $\sum_{q \in f} q$, where q denotes the natural atomic charges. The topological analysis of the ELF [41] and QTAIM [46,47] was performed using Multiwfn software [62]. The ELF localization domains (isovalue of 0.75 au) are represented from Paraview visualization software [63,64]. The calculations are performed using the Gaussian 03 package [65]. NCI analysis [66] was performed with the NCIPLOT4 program [67].

3. Results and Discussion

3.1. Analysis of the ELF Topology at the Ground State Electronic Structures of DAAs **7**–**10** *and NBD* **11**

ELF [41,42] topology allows quantitative characterization of chemical regions of a molecule, which is used to classify the TACs, and then to correlate their electronic structure with their molecular reactivity within the MEDT framework. Proposed by Domingo in 2019 [36], this standard classification of TACs into *pseudodiradical*, *pseudo(mono)radical*, carbenoid, or zwitterionic type has characterized 32CA reactions into *pmr-type*, *pdr-type*, *cb-type*, and *zw-type*, respectively, based on the respective TAC participation [36]. Herein, the ELF topology of DAAs **7**–**10** and NBD **11** is studied to assess their electronic structures. The ELF valence basin populations are given in Table 1, while the ELF basin attractor positions are shown in Figure 1.

Table 1. Electron localization function (ELF) valence basin populations, in average number of electrons e, at the MPWB1K/6-311G (d,p) optimized structures of DAAs **7**–**10** and NBD **11**.

	7	**8**	**9**	**10**	**11**
V(N1)	1.89	3.61	3.58	3.47	
V′(N1)	1.89				
V(N1,N2)	1.87	1.99	2.05	2.05	
V′(N1,N2)	1.87	1.89	1.85	1.92	
V(C3,N2)	3.01	2.90	2.88	2.82	
V(C3)	0.46	0.46	0.39	0.49	
V′(C3)	0.46	0.46	0.49	0.49	
V(C4,C5)					1.74
V′(C4,C5)					1.74
V(C6,C7)					1.74
V′(C6,C7)					1.74

The ELF topological analysis of DAAs **7**–**10** shows the presence of two monosynaptic basins, V(N1) and V′(N1), in **7** and one V(N1) monosynaptic basin in **8**–**10**, integrating a total population of 3.78 e (**7**), 3.61 e (**8**), 3.58 e (**9**), and 3.47 e (**10**), associated with the non-bonding electron density on N1 nitrogen; two disynaptic basins, V(N1,N2) and V′(N1, N2), integrating a total population of 3.74 e (**7**), 3.88 e (**8**), 3.90 e (**9**), and 3.97 e (**10**), associated with the N1–N2 double bond; and one V(C3,N2) disynaptic basin, integrating 3.01 e (**7**), 2.90 e (**9**), 2.88 e (**9**), and 2.82 e (**10**), associated with the C3–N2 overpopulated single bond, which shows the influence of substitution on the electronic distribution of the N1–N2–C3 moiety of these DAAs. Finally, the presence of two monosynaptic basins, V(C3) and V′(C3), integrating a total of 0.92 e (**7**), 0.92 e (**8**), 0.88 e (**9**), and 0.98 e (**10**), associated with a *pseudoradical* center at C3, classifies the DAAs **7**–**10** as *pseudo(mono)radical* TACs, thus suggesting their participation in *pmr-type* 32CA reactions [36].

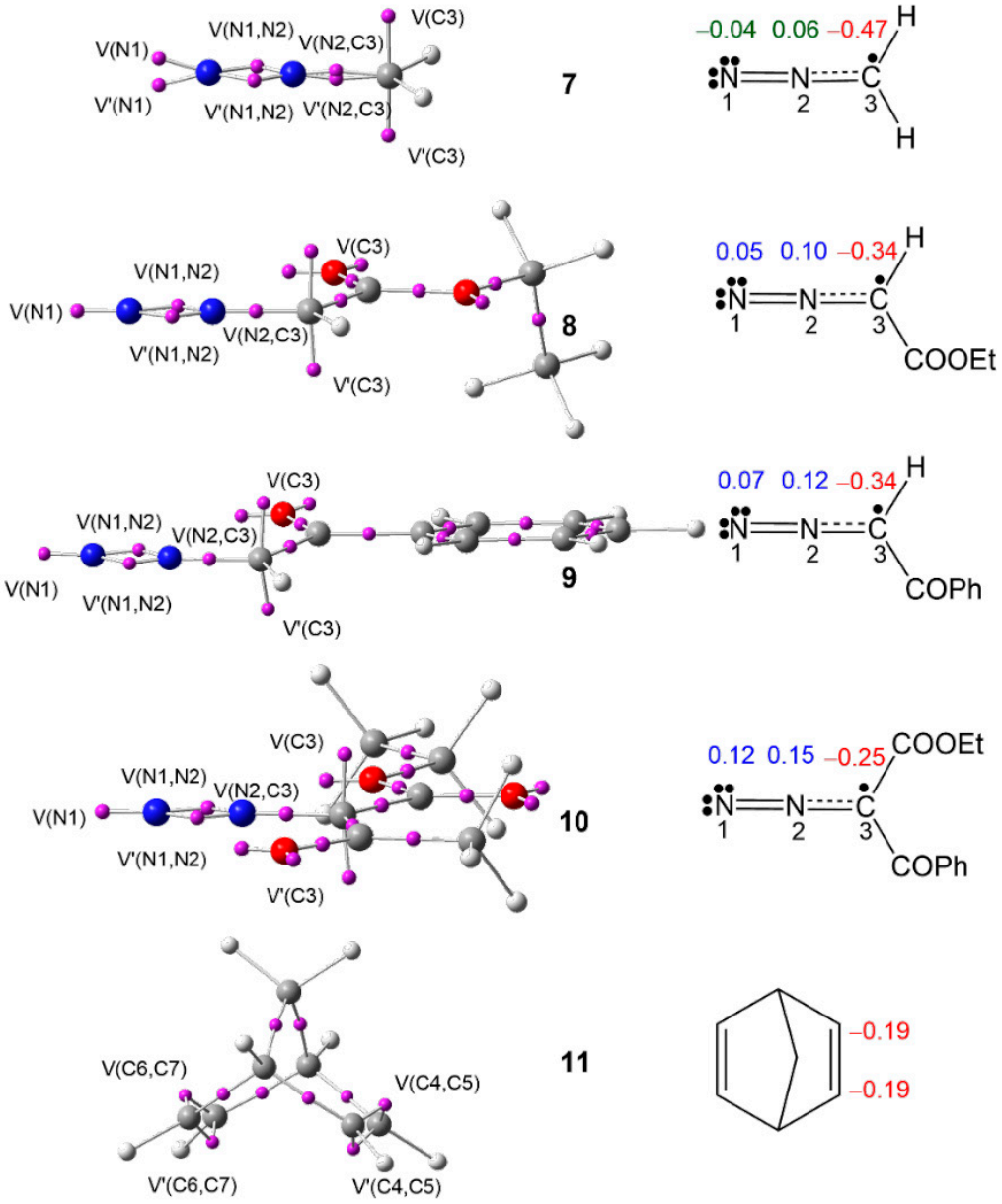

Figure 1. MPWB1K/6-311G(d,p) ELF basin attractor positions of DAAs **7**–**10** and NBD **11** and the proposed Lewis-like structures together with the natural atomic charges in average number of electrons e. Negative, negligible, and positive charges are shown in red, green, and blue colors, respectively.

ELF topology of NBD **11** shows the presence of two pairs of disynaptic basins, V(C4,C5) and V′(C4,C5), and V(C6,C7) and V′(C6,C7), integrating a total population of 3.48 e each pair, associated with the C4–C5 and C6–C7 double bonds of NBD **11**.

The proposed Lewis-like structures, together with the natural atomic charges of compounds **7**–**11**, are represented in Figure 1. The *pseudoradical* C3 carbon is negatively charged by −0.47 e (**7**), −0.34 e (**8**), −0.34 e (**9**), and −0.25 e (**10**), suggesting the influence of the EW substitution. The N1 and N2 nitrogen nuclei show negligible charges in simplest DAA **7**, while the N2 nitrogen shows a charge slightly greater than 0.10 e at DAAs **8**, **9**, and **10**. The charge distribution pattern in the DAAs **7**–**10** does not follow the commonly accepted 1,2-zwitterionic concept for DAAs.

3.2. Analysis of the CDFT Indices of DAAs **7**–**10** *and NBD* **11**

The analysis of the reactivity indices based on CDFT [43,44] has become a useful tool for studying reactivity in polar reactions [44]. Therefore, an analysis of CDFT reactivity indices was performed to predict the reactivity of the reagents in these 32CA reactions. The CDFT indices were calculated at the B3LYP/6-31G (d) computational level since it was used to define the electrophilicity and nucleophilicity scales [43,68,69]. The electronic chemical potential μ, chemical hardness η, electrophilicity ω, and nucleophilicity N indices of compounds **7**–**11** are gathered in Table 2. The MPWB1K/6-311G (d,p) reactivity indices are gathered in Table S3 in Supplementary Material.

Table 2. B3LYP/6-31G (d) electronic chemical potential μ, chemical hardness η, electrophilicity ω, and nucleophilicity N indices, in eV, of DAAs **7**–**10** and NBD **11**.

	μ	η	ω	*N*
DAA **10**	−4.58	4.87	2.15	2.09
DAA **8**	−4.27	4.79	1.90	2.45
DAA **9**	−4.20	4.76	1.85	2.53
DAA **7**	−3.63	4.70	1.40	3.13
NBD **11**	−2.94	5.88	0.74	3.23
ethylene **26**	−3.37	7.77	0.73	1.87

The electronic chemical potentials μ of DAAs **7**−**10**, μ = −3.63 (**7**), −4.27 (**8**), −4.20 (**9**), and −4.58 (**10**) eV, are lower than that of NBD **11**, μ = −2.94 eV, suggesting that along a polar process the electron density will flux from NBD **11** to DAAs **7**–**10** via reverse electron density flux (REDF) reactions [70].

The chemical hardness η of DAAs **7**–**10**, ranging from 4.70 to 4.87 eV, is also lower than that of NBD **11**, 5.88 eV, which means that the DAAs are more prone to electron density deformation than NBD **11**, i.e., they are softer. Interestingly, DAA **10**, having more EW substituents, is chemically harder than the simplest DAA **7**.

Within the electrophilicity scale [68], simplest DAA **7**, ω = 1.40 eV, is classified as a moderate electrophile, while DAAs **8**–**10**, ω > 1.85 eV, are classified as strong electrophiles. However, it is worth noting that among the strongly electrophilic DAAs, only DAA **10** would be electrophilically activated enough to work well experimentally, which is against the experimental findings. On the other hand, within the nucleophilicity scale [69], the simplest DAA **7**, N = 3.13 eV, is classified as a strong nucleophile, while DAAs **8**–**10**, N < 2.53 eV, are classified as moderate nucleophiles. As expected, the inclusion of EW groups at the C3 carbon of simplest DAA **7** increases the electrophilicity ω index and decreases the nucleophilicity N index of the DAA derivatives.

NBD **11** is classified as a marginal electrophile, ω = 0.74 eV, and a strong nucleophile, N = 3.23 eV. Both the strain caused by the bicyclic system and the presence of two C–C double bonds considerably increase the nucleophilicity N index of **11** with respect to that of ethylene **26**, N = 1.87 eV.

The analysis of the CDFT indices predicts that along a polar process, DAAs **7**–**10** will behave as electrophilic species while NBD **11** as the nucleophilic one. However, the experimental outcome [22] revealed that the EW substitution in the DAA decreases its reactivity towards NBD **11**. Along this series, the fastest 32CA reaction was that involving simplest DAA **7**, while strongly electrophilic DAA **10** having two EW –COOMe and –COPh groups was completely inactive. In addition, except for the reaction involving DAA **10**, CDFT predicts the other reactions to have a low-polar character as the DAAs are not sufficiently electrophilically activated. Thus, this CDFT analysis does not agree with the experimental results of this series of reactions.

A comparison of the B3LYP/6-31G (d) and MPWB1K/6-311G (d,p) reactivity indices shows that although they have different values, both computational levels give similar trends of reactivity.

3.3. Analysis of the Reaction Paths Associated with the 32CA Reactions between DAAs **7**–**10** *and NBD* **11**

Due to the molecular symmetry of the simplest DAA **7** and NBD **11**, two competitive stereoisomeric reaction paths are feasible for this 32CA reaction. They are related to the two approach modes of DAA **7** with respect to the two stereoisomeric faces of the C–C double bonds of NBD **11**. These reaction paths are called *syn* and *anti*. For DAAs **8**–**10**, which present a different substitution at the C3 carbon, two additional stereoisomeric reaction paths are feasible, the *endo* and the *exo* ones. Consequently, for the 32CA reactions involving DAAs **8**–**10**, four competitive reaction paths were considered (see Scheme 4). For the 32CA reaction of simplest DAA **7**, the *syn* and *anti* reaction paths lead to two diastereoisomeric pyrazolines **12** and **13**, respectively, via **TS1** and **TS2**. For the 32CA reactions involving substituted DAAs **8**–**10**, four diastereoisomeric pyrazolines **14**–**17**, **18**–**21**, and **22**–**25** can be formed via **TS3**–**TS6**, **TS7**–**TS10**, and **TS11**–**TS14**, respectively (Scheme 4). The four 32CA reactions follow a one-step mechanism. Relative electronic energies, enthalpies, entropies, and Gibbs free energies of the TSs and adducts are given in Table 3.

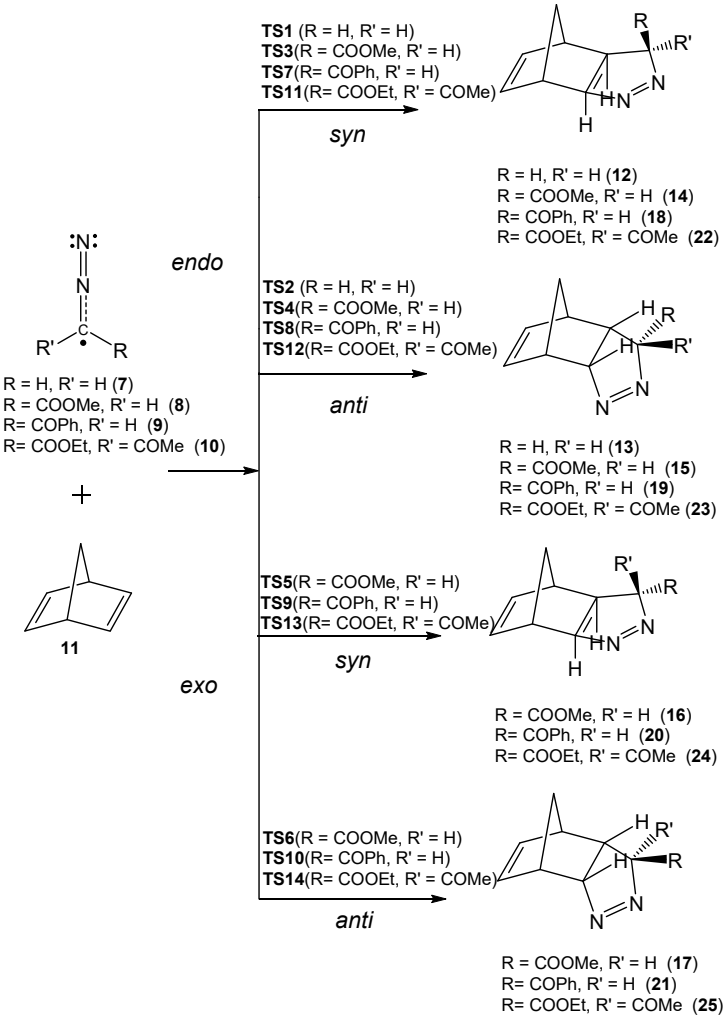

Scheme 4. Studied reaction paths for the 32CA reactions of DAAs **7**–**10** with NBD **11**.

From the energy results given in Table 3, a series of appealing conclusions can be obtained: (i) The gas phase activation energies associated with the energetically most favorable reaction paths of these 32CA reactions are found between 15.9 (**TS1**) and 23.3 (**TS11**) kcal·mol^{-1}; (ii) the increase of the activation energies in the order **TS1** (**7**) < **TS3** (**8**) < **TS10** (**9**) < **TS11** (**10**) is in complete agreement with the experimental outcomes [22];

(iii) these reactions are strongly exothermic by more than 30 kcal·mol^{-1}; (iv) inclusion of solvent effects increases the activation energies by between 0.3 (**TS11**) and 1.9 (**TS7**) kcal·mol^{-1}, and increases the exothermic character of the reactions by between 2.0 (**12**) and 4.1 (**22**) kcal·mol^{-1}. Formation of **18** is disfavored by 1.2 kcal·mol^{-1}; (v) inclusion of the thermal corrections increases the activation enthalpies in acetonitrile by between 0.8 (**TS3**) and 1.1 (**TS11**) kcal·mol^{-1} and decreases the reaction enthalpies by between 3.6 (**22**) and 4.8 (**12**) kcal·mol^{-1}; (vi) inclusion of entropies to enthalpies increases the activation Gibbs free energies in acetonitrile between 29.9 (**TS1**) and 43.0 (**TS14**) kcal·mol^{-1}, and decreases the reaction Gibbs free energies between −16.2 (**22**) and −37.1 (**12**) kcal·mol^{-1}; (vii) the strong exergonic character of these 32CA reactions makes them irreversible, and consequently, the products are obtained by kinetic control; (viii) the *syn*/*anti* facial stereoselectivity ranges from 0.7 (**7**) to 3.1 (**8**) kcal·mol^{-1}. While DAAs **7**, **8**, and **10** prefer the *syn* attack, DAA **9** prefers the *anti* one; and (ix) these 32CA reactions present a low *endo*/*exo* stereoselectivity; lower than 0.8 kcal·mol^{-1}. While the 32CA reactions of DAAs **7**, **8**, and **10** are *endo* selective, that of DAA **9** is *exo* selective.

Table 3. MPWB1K/6-311G (d,p) relative energies (ΔE, in kcal·mol^{-1}), enthalpies (ΔH, in kcal·mol^{-1}), entropies (ΔS, in cal·mol^{-1}K^{-1}), Gibbs free energies (ΔG, in kcal·mol^{-1}) and GEDT (in average number of electrons e) of TSs and pyrazolines for the 32CA reactions of DAAs **7**–**10** with NBD **11** (superscript 'a' refers to FEDF (forward electron density transfer) and superscript 'b' refers to REDF (reverse electron density transfer)).

	Gas Phase					Acetonitrile				
	ΔE	**ΔH**	**ΔS**	**ΔG**	**GEDT**	**ΔE**	**ΔH**	**ΔS**	**ΔG**	**GEDT**
TS1	15.9	16.8	−42.3	29.4	0.10 [a]	16.7	17.7	−40.8	29.9	0.10
12	−53.6	−49.0	−47.3	−34.8		−55.6	−50.8	−46.0	−37.1	
TS2	16.6	17.4	−42.9	30.2	0.12 [a]	17.6	18.5	−41.6	30.9	0.12
13	−52.9	−48.3	−47.5	−34.1		−55.2	−50.4	−46.1	−36.7	
TS3	18.9	19.4	−42.3	32.0	0.04	20.0	20.8	−42.5	33.5	0.03
14	−44.0	−40.3	−46.5	−26.4		−46.3	−42.1	−48.2	−27.7	
TS4	22.0	22.6	−44.1	35.7	0.04	23.3	24.1	−44	37.2	0.02
15	−42.1	−38.2	−49.2	−23.6		−45.3	−41.2	−49.2	−26.5	
TS5	19.5	20.1	−42.5	32.8	0.04	20.9	21.8	−44.1	35.0	0.03
16	−45.3	−41.4	−47.4	−27.3		−46.3	−42.1	−46.4	−28.3	
TS6	20.4	20.8	−41.4	33.2	0.06	21.9	22.5	−42.4	35.1	0.04
17	−44.1	−40.4	−43.5	−27.4		−45.9	−41.8	−45.8	−28.2	
TS7	21.4	22.0	−45.9	35.7	0.02	23.3	24.1	−47.0	38.1	0.01
18	−40.3	−37.2	−55.0	−20.8		−39.1	−35.0	−42.4	−22.4	
TS8	22.3	23.1	−48.3	37.5	0.05	24.0	24.7	−46.3	38.5	0.02
13	−39.5	−35.5	−52.2	−20.0		−42.4	−38.0	−52.2	−22.5	
TS9	21.7	22.5	−47.0	36.5	0.04	24.0	24.9	−46.8	38.8	0.02
20	−41.3	−37.3	−50.5	−22.2		−41.2	−37.1	−49.5	−22.3	
TS10	20.6	21.1	−46.0	34.8	0.05	22.8	23.5	−45.9	37.2	0.02
21	−44.6	−40.8	−51.1	−25.5		−43.8	−39.8	−50.1	−24.8	
TS11	23.3	24.2	−47.7	38.5	0.04	23.6	24.7	−47.8	38.9	0.08 [b]
22	−30.1	−26.8	−48.0	−12.5		−34.2	−30.6	−48.3	−16.2	
TS12	26.2	27-0	−48.5	41.4	0.04	26.7	27.6	−47.9	41.9	0.08 [b]
23	−35.1	−31.8	−49.9	−16.9		−36.3	−32.9	−51.2	−17.6	
TS13	23.9	24.2	−46.0	37.9	0.04	23.9	24.8	−46.1	38.6	0.08 [b]
24	−34.0	−30.8	−43.1	−18.0		−36.1	−32.6	−48.6	−18.1	
TS14	26.5	27.2	−49.5	41.9	0.03	26.9	27.9	−50.6	43.0	0.08 [b]
25	−31.5	−28.2	−50.6	−13.1		−34.4	−30.9	−49.2	−16.2	

The gas phase optimized geometries of the more favorable TSs are given in Figure 2, while the distances between the C–C and C–N interacting nuclei are given in Table 4. Some appealing conclusions can be drawn for these geometrical parameters: (i) Consider-

ing that C–C bond formation begins slightly earlier than the C–N one, [36] these distances at **TS1**–**TS10** indicate that, from a geometrical point of view, they correspond to hardly asynchronous TSs; (ii) a comparison of these distances at **TS11**–**TS14** with respect to those at the other TSs shows that the TSs involving DAA **10** are clearly more asynchronous. At **TS11**–**TS14**, the C–N distances are shorter, while the C–C ones are longer, suggesting more delayed C–C bond formation but more advanced C–N bond formation; i.e., more asynchronous processes; (iii) as all these distances are greater than 2.0 Å in the gas phase and acetonitrile, and considering that the C–C and C–N single bond formation take place at the short range of 2.0–1.9 and 1.9–1.8 Å, respectively, [36] they indicate that formation of the new C–C and C–N single bonds has not started yet at any TS (see Section 3.6); (iv) inclusion of solvent effects in the optimizations does not considerably modify the gas phase geometries. Note that for the 32CA reactions of DAAs **7**–**9**, these differences are lower than 0.02 Å.

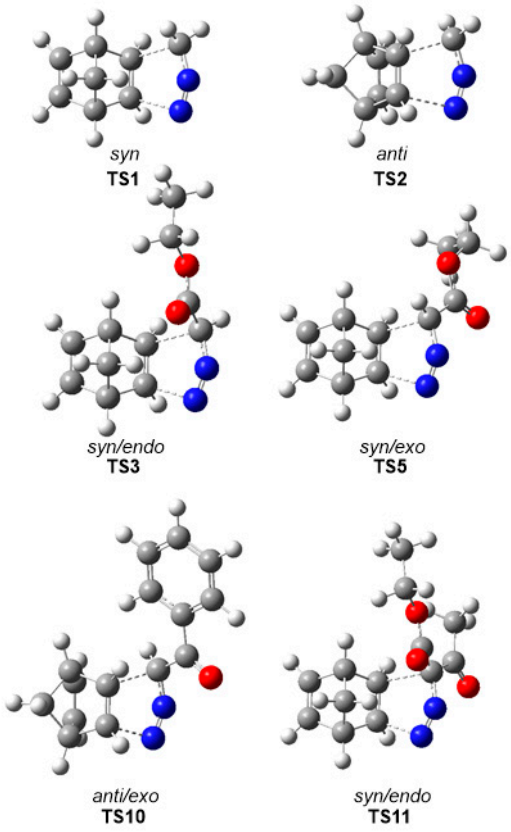

Figure 2. MPWB1K/6-311G (d,p) optimized geometries of some selected TSs associated with the 32CA reactions of DAAs **7**–**10** with NBD **11.**

Table 4. C–C and C–N distances, in angstroms Å, at the TSs involved in the 32CA reactions of DAAs **7**–**10** with NBD **11**, in the gas phase and in acetonitrile.

	C–C	C–N	C–C	C–N
	Gas Phase		*Acetonitrile*	
TS1	2.245	2.333	2.230	2.357
TS2	2.208	2.311	2.196	2.338
TS3	2.250	2.236	2.251	2.247
TS4	2.231	2.201	2.242	2.206
TS5	2.246	2.220	2.253	2.229
TS6	2.218	2.203	2.231	2.204
TS7	2.255	2.227	2.251	2.214
TS8	2.237	2.173	2.247	2.185
TS9	2.230	2.239	2.244	2.226
TS10	2.233	2.163	2.261	2.155
TS11	2.296	2.080	2.337	2.087
TS12	2.289	2.052	2.331	2.062
TS13	2.291	2.088	2.338	2.084
TS14	2.289	2.052	2.330	2.057

Finally, the GEDT at the TSs was calculated to assess the polarity of these 32CA reactions, and is given in Table 3. Reactions with GEDT values lower than 0.05 e correspond to non-polar processes, while values higher than 0.20 e correspond to polar processes. The 32CA reaction between simplest DAA **7** and NBD **11**, with GEDT of 0.10 e (**TS1**) and 0.12 (**TS2**), in the gas phase and in acetonitrile, is predicted as a 32CA reaction with some polar character, with the electron density fluxing from DAA **7** to NBD **11**. This GEDT analysis suggests that this 32CA reaction is classified as a forward electron density flux (FEDF) reaction [70]. Interestingly, this finding is against the analysis of the electronic chemical potential μ, electrophilicity ω, and nucleophilicity *N* indices of DAA **7** and NBD **11**, which predict that the reaction would not work experimentally but, if so, it should be a reaction of reverse electron density flux (REDF) [70] (see Table 2 and Section 3.2).

For the 32CA reactions of DAAs **8**–**10** with NBD **11**, the GEDT values are found between 0.02–0.05 e, predicting non-polar 32CA reactions, thus, being classified as reactions of null electron density flux (NEDF) [71]. This decrease in polarity is consistent with the increase in the energy barrier of the corresponding 32CA reactions. For the 32CA reaction of DAA **10** with NBD **11** in acetonitrile, which does not take place experimentally, the GEDT at the TSs is 0.08 e, showing a very low polar character. At this TS, the low electron density that fluxes from the NBD framework to the DAA ones, might permit to classify this 32CA reaction as a reaction of REDF [70]. However, note that this 32CA does not take place experimentally.

Interestingly, the 32CA reaction of simplest DAA **7**, the least electrophilic DAA of the series, with NBD **11** presents the highest GEDT. In addition, the electron density fluxes from DAA **7** to NBD **11**, against the analysis of the CDFT indices (see Section 3.2). Similar behavior was found along the *pdr-type* 32CA reaction between the simplest azomethine ylide and ethylene **26**, GEDT = 0.10 e [37], which was expected to be a reaction of NEDF. Note that neither NBD **11** nor ethylene **26** have any tendency to act as electrophiles. It seems that the presence of a non-bonding electron density at the ends of the TACs, which accounts for their high nucleophilic character, is responsible for the local electron density transfer taking place from these terminal carbon and nitrogen atoms to the double bonds of NBD **11** and ethylene **26**, a local phenomenon that cannot be anticipated by the analysis of the electronic chemical potential μ of the reagents.

3.4. NCI Analysis of the Preferred Anti/Exo Stereoselectivity in the 32CA Reaction of DAA **9** *with NBD* **11**

To understand the origin of the *anti/exo* stereoselectivity in the 32CA reaction of DAA **9** with NBD **11**, a comparative topological analysis of the attractive and repulsive NCIs taking

place at *syn/endo* **TS7** and *anti/exo* **TS10** was performed by means of the NCI approach. Note that the *syn/endo* stereoselectivity is preferred in every 32CA reaction except that involving DAA **9**. The corresponding isosurfaces are represented in Figure 3, while the plots of the reduced density gradient *s* vs. sign(λ_2) ρ(r) are given in Figure 4. A continuous color-coding scheme based on the second eigenvalue of the Hessian is used, where strong, attractive interactions are represented in blue, weak interactions in green, and strong repulsive interactions in red.

As can be observed in Figure 3, the surfaces associated with repulsive density overlap are greater than those associated with attractive interactions. This suggests that repulsive interactions have a greater role than the attractive ones in the preference for the *anti/exo* approach. A closer look reveals that considering only the surfaces associated with intermolecular interactions and skipping those associated with bond formation, the repulsive overlap spreads wider at **TS7** than at **TS10**.

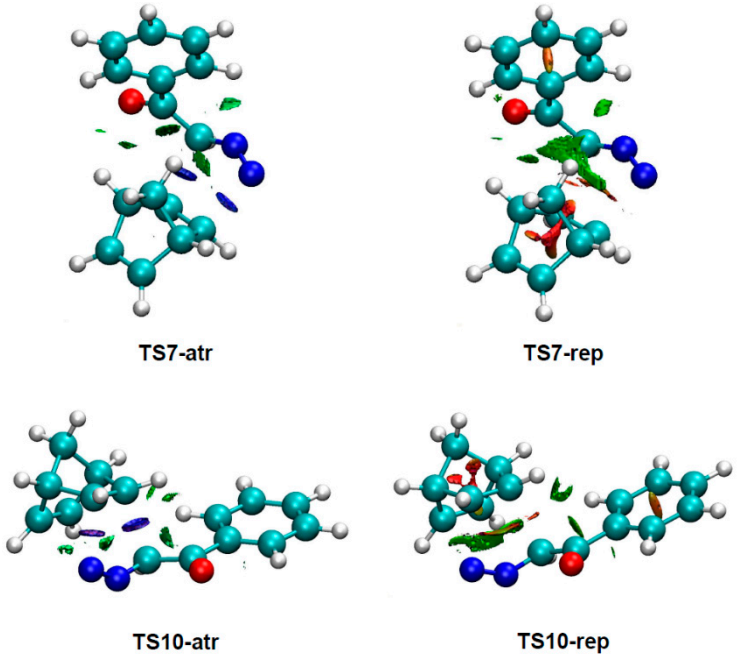

Figure 3. NCI isosurfaces associated with the attractive and repulsive density overlap at **TS7** and **TS10**. An isosurface value of 0.5 and a blue-green-red color scale from $-0.05 < \text{sign}(\lambda_2)\ \rho(r) < 0.05$ a.u. were used.

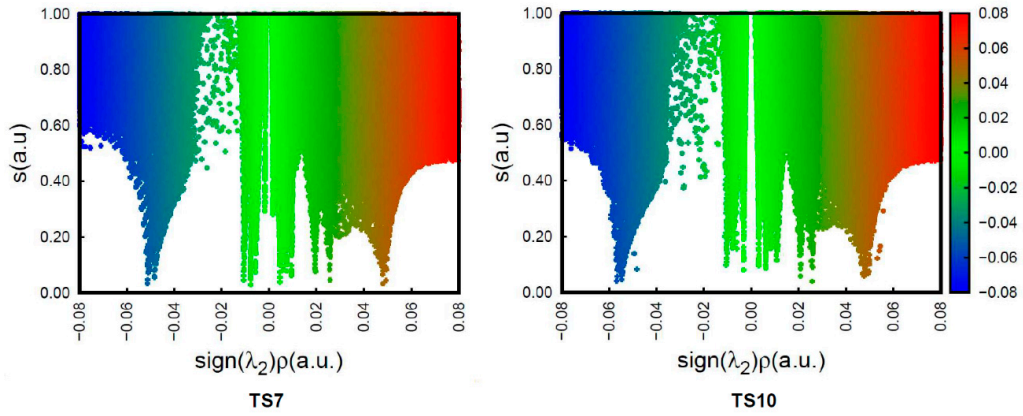

Figure 4. Plot of the reduced density gradient *s* vs. sign(λ_2) ρ for **TS7** and **TS10**.

The plots of the reduced density gradient *s* vs. sign(λ_2) ρ show that there are no qualitative differences between the density characteristics of the interactions (see Figure 4).

The only noticeable change is that the peaks associated with the weak NCIs, both the attractive and the repulsive ones, reach higher values of *s* at **TS10** than at **TS7**. This feature only indicates that these interactions are not associated with critical points in the electron density, [72] thus being only different in strength. Consequently, this analysis suggests that the weaker unfavorable interactions present at **TS10** are responsible for the *anti/exo* stereoselectivity in the 32CA reaction between DAA **9** and NBD **11**.

3.5. BET Study for the 32CA Reactions of DAAs **7** *and* **10** *with NBD* **11**

The BET has established the molecular mechanism of a great number of organic reactions by means of the analysis of the bonding changes along the reaction path, which is possible due to the straightforward connection between the electron density distribution and the chemical structure [42]. The detailed BET studies of the 32CA reactions of DAAs **7** and **10** with NBD **11** are given in the Supplementary Material in Sections 1 and 2. Herein, only the most relevant conclusions are analyzed and compared. The ELF basin attractor positions of the structures involved in the bond formation are shown in Figure 5.

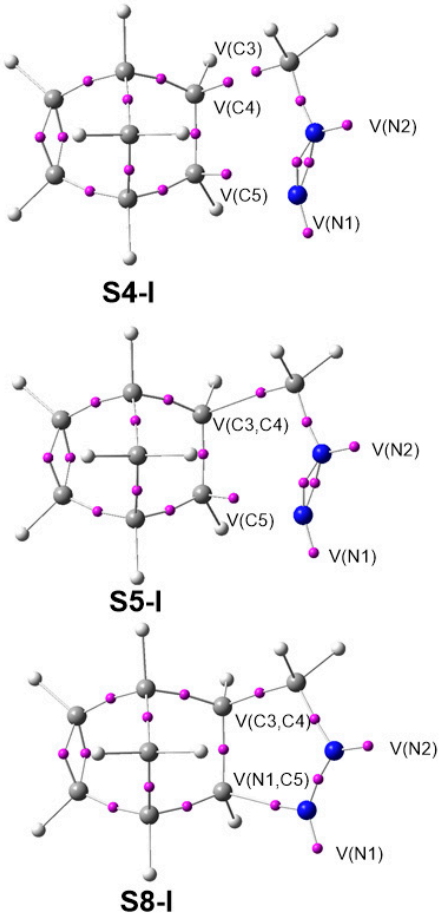

Figure 5. ELF basin attractor positions of **S4-I**, **S5-I** and **S8-I**, involved in the formation of the C3–C4 and N1–C5 single bonds.

From the BET study of the 32CA reaction of simplest DAA **7** with NBD **11**, we conclude that: (i) This 32CA reaction can be topologically divided into nine phases starting from structure **S0-I** and ending in pyrazoline **12**; (ii) *Phases I* and *II* are characterized by the depopulation of the N1–N2, N2–C3 and C4–C5 bonding regions. These changes in electron density demand an energy cost (EC) of 15.4 kcal mol^{-1}, which accounts for 97% of the activation energy needed to reach **TS1**, found in *Phase III*; (iii) the depopulation of these bonding regions creates the N2 nitrogen non-bonding electron density at structure **S1-I**, and the C4 and C5 *pseudoradical* centers at **S3-I** and **S4-I**, respectively (see **S4-I** in Figure 5);

(v) formation of the first C3–C4 single bond takes place at **S5-I**, by the C-to-C coupling of the two C3 and C4 *pseudoradical* centers present in **S4-I**, at a C–C distance of 2.05 Å and with an initial population of 1.36 e (see **S5-I** in Figure 5). Note that the C3 *pseudoradical* center was already present at DAA **7**; (vi) formation of the second N1–C5 single bond takes place at **S8-I**, by sharing part of the non-bonding electron density of the N1 nitrogen and that of the C5 *pseudoradical* center present in **S7-I**, at a C–N distance of 1.84 Å and with an initial population of 1.51 e (see **S8-I** in Figure 5); (vii) the formation of the second N1–C5 single bond begins when the first C3–C4 single bond formation has been completed by up to 93%, suggesting a *two-stage one-step* mechanism [73].

The BET study of the 32CA reaction of DAA **10** with NBD **11** draws some significant mechanistic conclusions: (i) This 32CA reaction can be divided into seven topological phases starting from **S0-II** and ending in pyrazoline **22**; (ii) *Phases I–III* are characterized by the depopulation of the N1–N2, N2–C3 and C4–C5 bonding regions. These changes in electron density demand an EC of 20.9 kcal mol^{-1}. This accounts for 90% of the activation energy needed to reach **TS11**, which is found in *Phase IV*; (iv) the depopulation of N1–N2 and N2–C3 bonding regions along *Phase I* creates the non-bonding electron density at N2 nitrogen at **S1-II**, while the depopulation of the C4–C5 bonding region along *Phases I–III* creates the C4 and C5 *pseudoradical* centers; (v) formation of the first C3–C4 single bond takes place at **S5-II**, by the C-to-C coupling of the two C3 and C4 *pseudoradical* centers present in **S4-II**, at a C–C distance of 2.11 Å, and with an initial population of 1.25 e. Note that the C3 *pseudoradical* center was already present at DAA **10**; (vii) formation of the second N1–C5 single bond takes place at **S6-II**, by sharing part of the non-bonding electron density of the N1 nitrogen and that of the C5 *pseudoradical* center present in **S5-I**, at a C–N distance of 1.82 Å, and with an initial population of 1.38 e; (vii) the formation of second N1–C5 single bond begins when the first C3–C4 single bond formation has been completed by up to 70%, suggesting an asynchronous one-step mechanism.

From this comparative analysis of the two BET studies, we conclude: (i) These 32CA reactions follow an asynchronous one-step mechanism, the highest asynchronicity in the bond formation being observed for the most favorable 32CA reaction of simplest DAA **7** with NBD **11**, which takes place via a *two-stage one-step* mechanism [73]. This finding confirms that any analysis based on the geometries of TSs, such as bond orders, is not suitable to assess the asynchronicity of a reaction; (ii) the initial phases of both 32CA reactions are related to the rupture of the N1–N2, N2–C3 and C4–C5 double bonds, demanded the formation of the N1, C3 and C5 non-bonding electron densities; (iii) while at the 32CA reaction involving simplest DAA **7** these bonding changes demand an EC of 15.4 kcal mol^{-1} with a GEDT of 0.10 e, at the 32CA involving DAA **10** these changes demand an EC of 20.9 kcal mol^{-1} with a GEDT of 0.01 e; and finally, (iv) formation of the C3–C4 single bond takes place before the N1–C5 bond formation, by coupling of two C3 and C4 *pseudoradical* centers. While the former is already present at the reagents, the latter is created along the reaction path. This behavior confirms the *pmr-type* mechanism [36].

3.6. ELF Study at the TSs Associated with the 32CA Reactions of DAAs **7**–**10** *with NBD* **11**

A comparative topological analysis of the ELF of the TSs involved in the 32CA reactions of DAAs **7**–**10** with NBD **11** was performed. The ELF valence basin populations at **TS1**–**TS14** associated with the 32CA reactions of DAAs **7**–**10** with NBD **11** are given in Table 5, while the ELF basin attractor positions of the *syn/endo* TSs, **TS1**, **TS3**, **TS7**, and **TS11**, are represented in Figure 6.

Table 5. ELF valence basin populations, in average number of electrons e, at the MPWB1K/6-311G (d,p) optimized at the TSs associated with the 32CA reactions of DAAs **7**–**10** with NBD **11.**

	V(N1)	V(N1,N2)	V′(N1,N2)	V(N2)	V(C3,N2)	V(C3)	V(C4,C5)
TS1	3.64	1.57	1.58	1.74	2.04	0.87	3.32
TS2	3.63	1.57	1.59	1.76	2.03	0.87	3.29
TS3	3.56	1.64	1.48	1.83	2.04	0.81	3.26
TS4	3.55	1.73	1.35	1.90	2.00	0.88	3.22
TS5	3.56	1.64	1.47	1.84	2.04	0.80	3.26
TS6	3.56	3.10		1.85	2.04	0.81	3.25
TS7	3.59	1.68	1.41	1.87	2.03	0.73	3.25
TS8	3.53	1.64	1.46	1.88	1.99	0.88	3.24
TS9	3.58	1.61	1.47	1.86	2.05	0.81	3.28
TS10	3.53	1.69	1.40	1.88	2.04	0.78	3.23
TS11	3.47	1.76	1.30	1.96	2.01	0.74	3.18
TS12	3.48	3.01		2.01	2.00	0.78	3.16
TS13	3.47	1.65	1.42	1.94	2.01	0.71	3.18
TS14	3.48	1.74	1.30	1.99	1.99	0.77	3.17

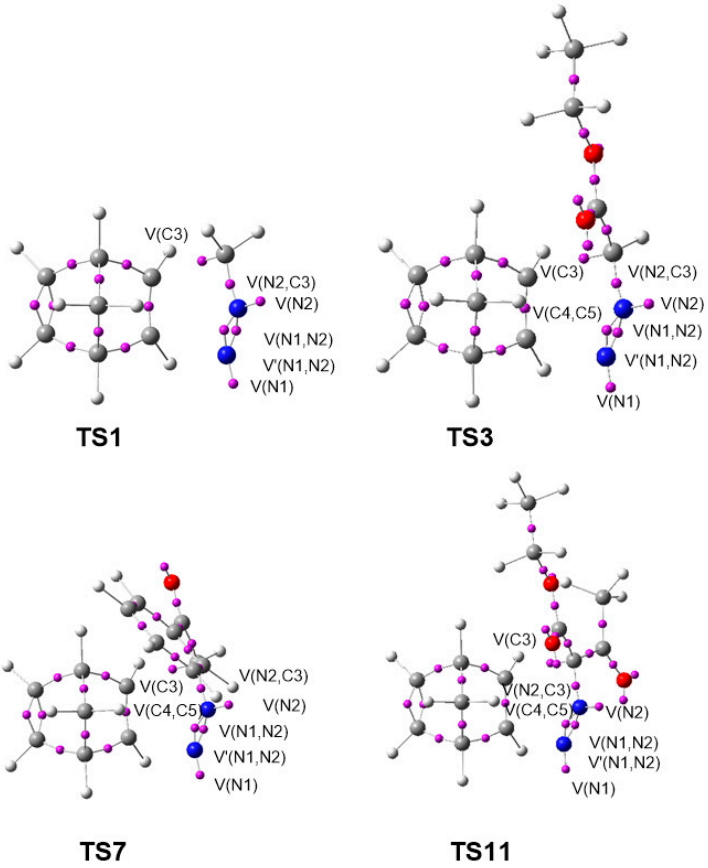

Figure 6. ELF basin attractor positions at the most favorable *endo*/*syn* TSs, **TS1**, **TS3**, **TS7**, and **TS11**.

TS1–**TS14** show the presence of a V(N2) monosynaptic basin integrating between 1.74 and 2.01 e, which is absent at the ground state electronic structures of the DAAs **7**–**10**. The V(N1,N2) and V′(N1,N2) disynaptic basins are depopulated from 3.74 e at DAA **7** to 3.15 e at **TS1** and 3.16 e at **TS2**, from 3.88 e at DAA **8** to 3.08–3.12 e at **TS3**–**TS6**, from 3.90 e at DAA **9** to 3.08–3.10 e at **TS7**–**TS10,** and from 3.97 e at DAA **10** to 3.01–3.07 e at **TS11**–**TS14**. On the other hand, the V(C3,N2) disynaptic basin integrating 3.01 e at DAA **7** is depopulated to 2.04 e at **TS1** and 2.03 e at **TS2**, from 2.90 e at **8** to 2.00–2.04 e at **TS3**–**TS6**, from 2.88 e at **9** to 1.99–2.05 e at **TS7**–**TS10**, and from 2.82 e at **10** to 1.99–2.01 e at

TS11–**TS14**. Thus, the N1–N2 and C3–N2 bonding regions are depopulated at the TSs to create the V(N2) monosynaptic basin associated with the N2 non-bonding electron density.

The V(C4,C5) and V′(C4,C5) disynaptic basins, integrating 3.48 e at NBD **11**, are merged into one V(C4,C5) disynaptic basin, integrating 3.16–3.32 e at the TSs, due to the depopulation of that region.

As shown in Figure 6, the four TSs, **TS1**, **TS3**, **TS7**, and **TS11**, present an identical electronic structure. Only small differences in the basin populations are observed as a consequence of the different substitutions at the DAA framework (see Table 5).

The activation energies of the TSs is, therefore, associated with the EC for the formation of the N2 non-bonding electron density and the rupture of C4–C5 double bond of NBD **11**. The TSs do not involve the formation of the new C3–C4 and N1–C5 single bonds, indicated by the absence of any V(C3,C4) and V(N1,C5) disynaptic basin. This is consistent with the distances between the C–C and N–C interacting centers, which are greater than 2 Å (see Figure 2) and the positive Laplacian of electron density at the bond critical points (BCPs) of the interatomic bonding regions at the TSs, discussed in Section 3.7.

3.7. Analysis of QTAIM Parameters at the TSs Associated with the 32CA Reactions of DAAs **7**–**10** *with NBD* **11**

Bader and coworkers [46,47] proposed the QTAIM concept to reveal the nature of interatomic interactions. Accordingly, the total electron density ρ and the Laplacian of electron density $\nabla^2\rho(r_c)$ are calculated at the BCPs **CP1** and **CP2** at the C3–C4 and N1–C5 bonding regions, respectively, and are given in Table 6. The total electron density accumulated at the BCPs is less than 0.1 a.u. and the Laplacian of electron density $\nabla^2\rho(r_c)$ shows small positive values in **TS1**–**TS14**, suggesting rather non-covalent interactions. Thus, the formation of the new C–C and N–C covalent bonds has not started yet at the TSs, which is in agreement with the topological analysis of the ELF (see Section 3.6).

Table 6. Total electron density, in average number of electrons e, ρ and Laplacian of electron density $\nabla^2\rho(r_c)$ at the BCPs **CP1** (C3–C4) and **CP2** (N1–C5) of the interatomic bonding regions in **TS1**–**TS14**.

	CP1 (C3–C4)		**CP2 (N1–C5)**	
	ρ	$\nabla^2\rho(r_c)$	ρ	$\nabla^2\rho(r_c)$
TS1	0.056	0.049	0.043	0.079
TS2	0.060	0.047	0.044	0.082
TS3	0.056	0.048	0.052	0.085
TS4	0.057	0.049	0.055	0.087
TS5	0.057	0.047	0.053	0.086
TS6	0.059	0.045	0.055	0.088
TS7	0.054	0.049	0.053	0.085
TS8	0.057	0.046	0.058	0.089
TS9	0.058	0.046	0.052	0.084
TS10	0.058	0.045	0.059	0.089
TS11	0.052	0.048	0.070	0.087
TS12	0.052	0.048	0.073	0.088
TS13	0.052	0.048	0.069	0.087
TS14	0.053	0.047	0.073	0.088

3.8. Analysis of the Origin of the Deceleration of These 32CA Reactions with the Increase of the EW Character of the Substituents Present in These DAA

Many MEDT studies of cycloaddition reactions have shown that the activation energies of non-polar and polar reactions are mainly associated with the EC demanded the depopulation, i.e., rupture, of the X–Y double bond regions involved in the reaction [36]. In polar reactions, this EC is decreased by the GEDT taking place along the reaction path [74]. The very low GEDT found at the TSs associated with the 32CA reactions of DAA **8**–**10**, lower than 0.05 e (see Table 3), indicates that they have a non-polar character. Consequently, the corresponding activation energies can mainly be associated with the

changes in electron density in the N1–N2–C3 and C4–C5 bonding regions. Analysis of the total population of the V(N1), V′(N1), V(N1,N2), V′(N1,N2), and V(C3,N2) valence basins of DAAs **7–10**, 3.01 e **7**, 2.90 e **8**, 2.88 e **9**, and 2.82 e **10**, shows a continuous depopulation of the N1–N2–C3 bonding region of these TACs with the increase of the EW character of the substituents present at the C3 carbon (see Table 1).

Interestingly, as Figure 7 shows, a very good correlation between the total populations of the V(N1), V′(N1), V(N1,N2), V′(N1,N2), and V(C3,N2) valence basins and the activation energies of these 32CA reactions can be established (R^2 = 0.98).

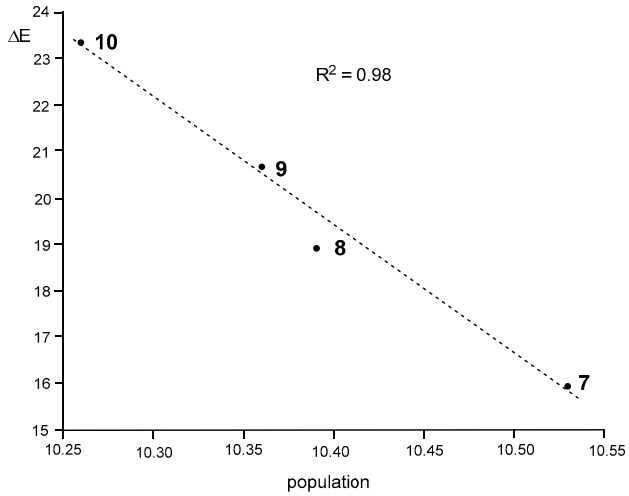

Figure 7. A plot of the activation energies of the 32CA reactions between DAA **7–10** and NBD **11**, ΔE_{act}, in kcal·mol^{-1}, vs. the total electron density population of the N1–N2–C3 bonding region of DAA **7–10**, in average number of e.

As can be seen, the activation energies of this series of 32CA reactions linearly increase with the depopulation of the N1–N2–C3 bonding region, which could be understood as a drawback to using the electron density needed for the formation of the new bonds. Consequently, the lowest population found at the disubstituted DAA **10** provokes that the corresponding 32CA reaction presents the highest EC for the bonding changes, thus presenting the highest activation energy (see Section 3.3). Note that the chemical hardness of **10** is the highest (see Table 1). This finding justifies the observation that the 32CA reaction involving the most electrophilic species of this series does not take place experimentally.

4. Conclusions

The 32CA reactions of NBD **11** with simplest DAA **7** and three substituted DAAs **8–10** of increased electrophilic character, experimentally reported by Huisgen, [22] have been studied at MPWB1K/6-311G (d,p) level of theory within the MEDT framework.

Topological analysis of the ELF at the ground state electronic structures of DAAs **7–10** characterizes these TACs as *pseudo(mono)radical* ones, participating in *pmr-type* 32CA reactions.

Analysis of the CDFT indices predicts the strong nucleophilicity of NBD **11**, while DAAs **7–10** are predicted to be electrophilic reagents. Contrary to the CDFT analysis, these *pmr-type* 32CA reactions experimentally show a decrease in reactivity with the introduction of EW substituents, the most electrophilic DAA **10** being completely inactive towards NBD **11**.

These 32CA reactions are exergonic. The calculated activation enthalpies are found from 17.7 to 27.9 kcal mol^{-1} in acetonitrile. The 32CA reaction of simplest DAA **7**, predicted as the least electrophilic DAA, with NBD **11**, shows the lowest activation enthalpy, while the activation parameters increase progressively from the 32CA reaction with DAA **7** to that with DAA **10**, in complete agreement with the experimental outcomes. The *syn/endo* attack is preferred over the *anti/exo* one in every case except DAA **9**. An NCI analysis suggested that the weaker unfavorable interactions taking place at the corresponding

anti/exo approach than at the *syn/endo* are responsible for that preference. Interestingly, the highest GEDT is found for the fastest 32CA reaction between DAA **7** and NBD **11**, indicating a low polar FEDF process with electron density flux from DAA **7** to NBD **11**, while the reaction with DAA **10**, the most electrophilic species, is characterized as a NEDF process, contrary to the CDFT prediction.

BET study shows that the activation energies of the 32CA reactions of DAAs **7** and **10** with NBD **11** are mainly due to the rupture of the C4–C5 double bond of NBD **11** and the formation of non-bonding electron density at the N2 of the DAAs. The topological analysis of the ELF at the TSs and QTAIM parameters indicate that the formation of C3–C4 and N1–C5 covalent bonds has not started yet at any TS.

This MEDT study concludes that for the series of 32CA reactions of NBD **11** with substituted DAAs **7**–**10** of increased electrophilic character, the analysis based on CDFT indices does not account for the experimental outcomes. A good linear correlation between the populations of the N–N–C core of these DAAs and the activation energies associated with the corresponding *pmr-type* 32CA reactions is established, indicating that the depopulation of the N–N–C framework of the DAAs, considered an obstacle to the bond formation, is responsible for the experimentally found deceleration.

Supplementary Materials: The following are available online https://www.mdpi.com/2624-8549/3/1/6/s1.

Author Contributions: Conceptualization, L.R.D., M.R.-G. and N.A.; methodology, L.R.D., M.R.-G. and N.A.; software L.R.D., M.R.-G. and N.A.; validation, L.R.D., M.R.-G. and N.A.; formal analysis, L.R.D., M.R.-G. and N.A.; investigation L.R.D., M.R.-G. and N.A.; resources, L.R.D., M.R.-G. and N.A.; data curation, M.R.-G. and N.A.; writing—original draft preparation, M.R.-G. and N.A.; writing—review and editing, L.R.D., M.R.-G. and N.A..; visualization, L.R.D., M.R.-G. and N.A.; supervision, L.R.D.; project administration, L.R.D.; funding acquisition, L.R.D. All authors have read and agreed to the published version of the manuscript.

Funding: LRD is grateful to the Ministerio de Ciencias e Innovación (MICINN) of the Spanish Government for the project PID2019-110776GB-I00 (AEI/FEDER, UE). This project has also received funding from the European Union's Horizon 2020 research and innovation programme under the Marie Skłodowska-Curie grant agreement No. 846181 (MRG).

Institutional Review Board Statement: Not applicable.

Informed Consent Statement: Not applicable.

Data Availability Statement: Data is contained within the article or supplementary material.

Conflicts of Interest: The authors declare no conflict of interest.

References

1. Flid, V.R.; Gringolts, M.L.; Shamsiev, R.S.; Finkelshtein, E.S. Norbornene, norbornadiene and their derivatives: Promising semi-products for organic synthesis and production of polymeric materials. *Russ. Chem. Rev.* **2018**, *87*, 1169. [CrossRef]
2. Corey, E.J.; Shibasaki, M.; Nicolaou, K.C.; Malmsten, C.L.; Samuelsson, B. Simple, stereocontrolled total synthesis of a biologically active analog of the prostaglandin endoperoxides (PGH2, PGG2). *Tetrahedron Lett.* **1976**, *17*, 737–740. [CrossRef]
3. Lee, M.; Ikeda, I.; Kawabe, T.; Mori, S.; Kanematsu, K. Enantioselective Total Synthesis of cis-Trikentrin B. *J. Org. Chem.* **1996**, *61*, 3406–3416. [CrossRef]
4. Rosa, C.D.; Malafronte, A.; Auriemma, F.; Scoti, M.; Girolamo, R.D.; D'Alterio, M.C.; Ricci, G.; Zanchin, G.; Leone, G. Synthesis, chain conformation and crystal structure of poly(norbornadiene) having repeating 3,5-enchained nortricyclene units. *Polym. Chem.* **2019**, *10*, 4593–4603. [CrossRef]
5. Petersen, A.U.; Hofmann, A.I.; Fillols, M.; Mansø, M.; Jevric, M.; Wang, Z.; Sumby, C.J.; Müller, C.; Moth-Poulsen, K. Solar Energy Storage by Molecular Norbornadiene–Quadricyclane Photoswitches: Polymer Film Devices. *Adv. Sci.* **2019**, *6*, 1900367. [CrossRef] [PubMed]
6. Daştan, A.; Balci, M. High temperature bromination. Part 18: Bromination of benzonorbornadiene derivatives: Polybrominated-benzonorbornenes and benzonorbornadienes. *Tetrahedron* **2005**, *61*, 5481–5488. [CrossRef]
7. Horasan, N.; Kara, Y.; Azizoğlu, A.; Balci, M. Low and high temperature bromination of exocyclic dienes: High temperature bromination. Part 16. *Tetrahedron* **2003**, *59*, 3691–3699. [CrossRef]

8. Altundas, R.; Dastan, A.; Ünaldi, N.S.; Güven, K.; Uzun, O.; Balci, M. The Di-π-methane Photorearrangement of 2,3-Disubstituted Benzobarrelenes and Benzonorbornadiene—Substituent Effects in Regioselectivity. *Eur. J. Org. Chem.* **2002**, 526–533. [CrossRef]
9. Nişancı, B.; Dalkılıç, E.; Güney, M.; Daştan, A. Synthesis and Diels–Alder cycloaddition reaction of norbornadiene and benzonorbornadiene dimers. *Beilstein J. Org. Chem.* **2009**, *5*, 39. [CrossRef]
10. Khan, R.; Chen, J.; Fan, B. Versatile Catalytic Reactions of Norbornadiene Derivatives with Alkynes. *Adv. Synth. Catal.* **2020**, *362*, 1564. [CrossRef]
11. Cristina, D.; Amici, M.D.; Micheli, C.D.; Gandolfi, R. Site selectivity in the reactions of 1,3-dipoles with norbornadiene derivatives. *Tetrahedron* **1981**, *37*, 1349–1357. [CrossRef]
12. Aggarwal, V.K.; Roseblade, S.J.; Barrell, J.K.; Alexander, R. Highly stereoselective nitrone cycloaddition onto a chiral ketene equivalent: Asymmetric synthesis of cispentacin. *Org. Lett.* **2002**, *4*, 1227–1229. [CrossRef] [PubMed]
13. Maiuolo, L.; Nino, A.D. Synthesis of isoxazolidines by 1, 3-dipolar cycloaddition: Recent advances. *Targets Heterocycl. Syst.* **2015**, *19*, 299–345.
14. Rück-Braun, K.; Freysoldt, T.H.E.; Wierschem, F. 1,3-Dipolar cycloaddition on solid supports: Nitrone approach towards isoxazolidines and isoxazolines and subsequent transformations. *Chem. Soc. Rev.* **2005**, *34*, 507–516. [CrossRef] [PubMed]
15. Ali, S.A.; Saeed, M.T.; Rahman, S.U. The isoxazolidines: A new class of corrosion inhibitors of mild steel in acidic medium. *Corros. Sci.* **2003**, *45*, 253–266. [CrossRef]
16. Yip, C.; Handerson, S.; Tranmer, G.K.; Tam, W. Intramolecular 1,3-Dipolar Cycloadditions of Norbornadiene-Tethered Nitrile Oxides. *J. Org. Chem.* **2001**, *66*, 276–286. [CrossRef] [PubMed]
17. Tranmer, G.K.; Tam, W. Intramolecular 1,3-Dipolar Cycloadditions of Norbornadiene-Tethered Nitrones. *J. Org. Chem.* **2001**, *66*, 5113–5123. [CrossRef]
18. Tajabadi, J.; Bakavoli, M.; Gholizadeh, M.; Eshghi, H.; Izadyar, M. The origin of regio- and stereoselectivity in the 1,3-dipolar cycloaddition of nitrile oxides with C1-substituted 7-oxabenzonorbornadienes, a DFT study. *RSC Adv.* **2015**, *5*, 38489–38498. [CrossRef]
19. Adjieufack, A.I.; Ndassa, I.M.; Mbadcam, J.K.; Ríos-Gutiérrez, M.; Domingo, L.R. Steric interactions controlling the syn stereofacial selectivity in the [3 + 2] cycloaddition reaction between acetonitrile oxide and 7-oxanorborn-5-en-2-ones: A molecular electron density theory study. *J. Phys. Org. Chem.* **2017**, *30*, e3710. [CrossRef]
20. Arhin, G.; Adams, A.H.; Opoku, E.; Tia, R.; Adei, E. 1,3-Dipolar cycloaddition reactions of selected 1,3-dipoles with 7-isopropylidenenorbornadiene and follow-up thermolytic cleavage: A computational study. *J. Mol. Graph. Model.* **2019**, *92*, 267–279. [CrossRef]
21. Opoku, E.; Arhin, G.; Pipim, G.B.; Adams, A.H.; Tia, R.; Adei, E. Site-, enantio- and stereo-selectivities of the 1,3-dipolar cycloaddition reactions of oxanorbornadiene with C,N-disubstituted nitrones and dimethyl nitrilimines: A DFT mechanistic study. *Theor. Chem. Acc.* **2020**, *139*, 16. [CrossRef]
22. Huisgen, R. Kinetics and mechanism of 1,3-dipolar cycloadditions. *Angew. Chem., Int. Ed.* **1963**, *2*, 633–696. [CrossRef]
23. Huisgen, R. Altes und Neues über aliphatische Diazoverbindungen. *Angew. Chem.* **1955**, *67*, 439–463. [CrossRef]
24. Fukui, K. *Molecular Orbitals in Chemistry, Physics, and Biology*; Academic Press: New York, NY, USA, 1964; p. 525.
25. Domingo, L.R. Molecular electron density theory. *Molecules.* **2016**, *21*, 1319. [CrossRef]
26. Domingo, L.R.; Acharjee, N. Molecular Electron Density Theory: A New Theoretical Outlook on Organic Chemistry. In *Frontiers in Computational Chemistry*; Ul-Haq, Z., Wilson, A.K., Eds.; Bentham and Science: Singapore, 2020; Volume 5, pp. 174–227. [CrossRef]
27. Domingo, L.R.; Acharjee, N. Unravelling the strain-promoted [3 + 2] cycloaddition reactions of phenyl azide with cycloalkynes from the molecular electron density theory perspective. *New J. Chem.* **2020**, *44*, 13633–13643. [CrossRef]
28. Domingo, L.R.; Acharjee, N. Unveiling the high reactivity of strained dibenzocyclooctyne in [3 + 2] cycloaddition reactions with diazoalkanes through the molecular electron density theory. *J. Phys. Org. Chem.* **2020**, *33*, e4100. [CrossRef]
29. Domingo, L.R.; Ríos-Gutiérrez, M.; Pérez, P. A Molecular Electron Density Theory Study of the Reactivity and Selectivities in [3 + 2] Cycloaddition Reactions of C,N-Dialkyl Nitrones with Ethylene Derivatives. *J. Org. Chem.* **2018**, *83*, 2182–2197. [CrossRef]
30. Domingo, L.R.; Ríos-Gutiérrez, M.; Acharjee, N. A Molecular Electron Density Theory Study of the Chemoselectivity, Regioselectivity, and Stereofacial Selectivity in the Synthesis of an Anticancer Spiroisoxazoline derived from α-Santonin. *Molecules* **2019**, *24*, 832. [CrossRef]
31. Domingo, L.R.; Ríos-Gutiérrez, M.; Adjieufack, A.I.; Ndassa, I.M.; Nouhou, C.N.; Mbadcam, J.K. Molecular Electron Density Theory Study of Fused Regioselectivity in the Intramolecular [3 + 2] Cycloaddition Reaction of Nitrones. *ChemistrySelect* **2018**, *3*, 5412–5420. [CrossRef]
32. Domingo, L.R.; Acharjee, N. [3 + 2] Cycloaddition Reaction of C-Phenyl-N-methyl Nitrone to Acyclic-Olefin-Bearing-Electron-Donating Substituent: A Molecular Electron Density Theory Study. *Chemistryselect* **2018**, *3*, 8373–8380. [CrossRef]
33. Gutiérrez, M.R.; Nasri, L.; Nacereddine, A.K.; Djerourou, A.; Domingo, L.R. A molecular electron density theory study of the [3 + 2] cycloaddition reaction between an azomethine imine and electron deficient ethylenes. *J. Phys. Org. Chem.* **2018**, *31*, e3830. [CrossRef]
34. Domingo, L.R.; Ríos-Gutiérrez, M.; Pérez, P. A Molecular Electron Density Theory Study of the Role of the Copper-Metallation of AzomethineYlides in [3 + 2] Cycloaddition Reactions. *J. Org. Chem.* **2018**, *83*, 10959–10973. [CrossRef] [PubMed]
35. Domingo, L.R.; Acharjee, N. A molecular electron density theory study of the Grignard reagent mediated regioselective direct synthesis of 1,5-disubstituted-1,2,3-triazoles. *J. Phys. Org. Chem.* **2020**, *33*, e4062. [CrossRef]

36. Ríos-Gutiérrez, M.; Domingo, L.R. Unravelling the mysteries of the [3 + 2] cycloaddition reactions. *Eur. J. Org. Chem.* **2019**, 267–282. [CrossRef]
37. Domingo, L.R.; Chamorro, E.; Pérez, P. Understanding the High Reactivity of the Azomethine Ylides in [3 + 2] Cycloaddition Reactions. *Lett. Org. Chem.* **2010**, *7*, 432–439. [CrossRef]
38. Domingo, L.R.; Ríos-Gutiérrez, M. A Molecular Electron Density Theory Study of the Reactivity of Azomethine Imine in [3 + 2] Cycloaddition Reactions. *Molecules.* **2017**, *22*, 750. [CrossRef]
39. Ríos-Gutiérrez, M.; Domingo, L.R. The carbenoid-type reactivity of simplest nitrile imine from a molecular electron density theory perspective. *Tetrahedron* **2019**, *75*, 1961–1967. [CrossRef]
40. Domingo, L.R.; Ríos-Gutiérrez, M.; Emamian, S. Understanding the domino reactions between 1-diazopropan-2-one and 1,1-dinitroethylene. A molecular electron density theory study of the [3 + 2] cycloaddition reactions of diazoalkanes with electron-deficient ethylenes. *RSC Adv.* **2017**, *7*, 15586–15595. [CrossRef]
41. Becke, A.D.; Edgecombe, K.E. A simple measure of electron localization in atomic and molecular systems. *J. Chem. Phys.* **1990**, *92*, 5397–5403. [CrossRef]
42. Silvi, B.; Savin, A. Classification of chemical bonds based on topological analysis of electron localization functions. *Nature* **1994**, *371*, 683–686. [CrossRef]
43. Parr, R.G.; Yang, W. *Density Functional Theory of Atoms and Molecules*; Oxford University Press: New York, NY, USA, 1989.
44. Domingo, L.R.; Ríos-Gutiérrez, M.; Pérez, P. Applications of the Conceptual Density Functional Theory Indices to Organic Chemistry Reactivity. *Molecules* **2016**, *21*, 748. [CrossRef] [PubMed]
45. Krokidis, X.; Noury, S.; Silvi, B. Characterization of Elementary Chemical Processes by Catastrophe Theory. *J. Phys. Chem. A* **1997**, *101*, 7277–7282. [CrossRef]
46. Bader, R.F.W. *Atoms in Molecules: A Quantum Theory*; Clarendon Press: Oxford, UK, 1990.
47. Bader, R.F.W.; Essén, H. The characterization of atomic interactions. *J. Chem. Phys.* **1984**, *80*, 1943–1960. [CrossRef]
48. Schlegel, H.B. Optimization of equilibrium geometries and transition structures. *J. Comput. Chem.* **1982**, *3*, 214–218. [CrossRef]
49. Zhao, Y.; Truhlar, D.G. Hybrid Meta Density Functional Theory Methods for Thermochemistry, Thermochemical Kinetics, and Noncovalent Interactions: The MPW1B95 and MPWB1K Models and Comparative Assessments for Hydrogen Bonding and van der Waals Interactions. *J. Phys. Chem. A* **2004**, *108*, 6908–6918. [CrossRef]
50. Hehre, W.J.; Radom, L.; Schleyer, P.V.R.; Pople, J. *Ab initio Molecular Orbital Theory*; Wiley: New York, NY, USA, 1986.
51. Fukui, K. Formulation of the reaction coordinate. *J. Phys. Chem.* **1970**, *74*, 4161–4163. [CrossRef]
52. González, C.; Schlegel, H.B. Reaction path following in mass-weighted internal coordinates. *J. Phys. Chem.* **1990**, *94*, 5523–5527. [CrossRef]
53. González, C.; Schlegel, H.B. Improved algorithms for reaction path following: Higher-order implicit algorithms. *Chem. Phys.* **1991**, *95*, 5853–5860. [CrossRef]
54. Tomasi, J.; Persico, M. Molecular Interactions in Solution: An Overview of Methods Based on Continuous Distributions of the Solvent. *Chem. Rev.* **1994**, *94*, 2027–2094. [CrossRef]
55. Simkin, B.I.A.; Sheikhet, I.I. *Quantum Chemical and Statistical Theory of Solutions: A Computational Approach*; Ellis Horwood: London, UK, 1995.
56. Cossi, M.; Barone, V.; Cammi, R.; Tomasi, J. Ab Initio Study of Solvated Molecules: A New Implementation of the Polarizable Continuum Model. *Chem. Phys. Lett.* **1996**, *255*, 327–335. [CrossRef]
57. Cances, E.; Mennucci, B.; Tomasi, J. A new integral equation formalism for the polarizable continuum model: Theoretical background and applications to isotropic and anisotropic dielectrics. *J. Chem. Phys.* **1997**, *107*, 3032–3041. [CrossRef]
58. Barone, V.; Cossi, M.; Tomasi, J. Geometry optimization of molecular structures in solution by the polarizable continuum model. *J. Comput. Chem.* **1998**, *19*, 404–417. [CrossRef]
59. Domingo, L.R. A new C–C bond formation model based on the quantum chemical topology of electron density. *RSC Adv.* **2014**, *4*, 32415–32428. [CrossRef]
60. Reed, A.E.; Weinstock, R.B.; Weinhold, F. Natural population analysis. *J. Chem. Phys.* **1985**, *83*, 735–746. [CrossRef]
61. Reed, A.E.; Curtiss, L.A.; Weinhold, F. Intermolecular interactions from a natural bond orbital, donor-acceptor viewpoint. *Chem. Rev.* **1988**, *88*, 899–926. [CrossRef]
62. Lu, T.; Chen, F. Multiwfn: A multifunctional wavefunction analyzer. *J. Comp. Chem.* **2012**, *33*, 580–592. [CrossRef]
63. Ahrens, J.; Geveci, B.; Law, C. *ParaView: An End-User Tool for Large Data Visualization*; Visualization Handbook; Elsevier: Amsterdam, The Netherlands, 2005.
64. Ayachit, U. *The ParaView Guide: A Parallel Visualization Application*; Kitware: New York, NY, USA, 2015.
65. Frisch, M.J.; Trucks, G.W.; Schlegel, H.B.; Scuseria, G.E.; Robb, M.A.; Cheeseman, J.R.; Scalmani, G.; Barone, V.; Petersson, G.A.; Nakatsuji, H.; et al. *Gaussian 16*; Gaussian, Inc.: Wallingford, CT, USA, 2016.
66. Johnson, E.R.; Keinan, S.; Mori-Sánchez, P.; Contreras-García, J.; Cohen, A.J.; Yang, W. Revealing noncovalent interactions. *J. Am. Chem. Soc.* **2010**, *132*, 6498–6506. [CrossRef]
67. Boto, R.A.; Peccati, F.; Laplaza, R.; Quan, C.; Carbone, A.; Piquemal, J.P.; Maday, Y.; Contreras-García, J. NCIPLOT4: Fast, Robust, and Quantitative Analysis of Noncovalent Interactions. *J. Chem. Theory Comput.* **2020**, *16*, 4150–4158. [CrossRef]
68. Domingo, L.R.; Aurell, M.J.; Pérez, P.; Contreras, R. Quantitative characterization of the global electrophilicity power of common diene/dienophile pairs in Diels–Alder reactions. *Tetrahedron* **2002**, *58*, 4417–4423. [CrossRef]

69. Jaramillo, P.; Domingo, L.R.; Chamorro, E.; Pérez, P. A further exploration of a nucleophilicity index based on the gas-phase ionization potentials. *J. Mol. Struct. Theochem.* **2008**, *865*, 68–72. [CrossRef]
70. Domingo, L.R.; Ríos-Gutiérrez, M.; Pérez., P. A molecular electron density theory study of the participation of tetrazines in aza-Diels–Alder reactions. *RSC Adv.* **2020**, *10*, 15394–15405. [CrossRef]
71. Domingo, L.R.; Kula, K.; Ríos-Gutiérrez, M. Unveiling the Reactivity of Cyclic AzomethineYlides in [3 + 2] Cycloaddition Reactions within the Molecular Electron Density Theory. *Eur. J. Org. Chem.* **2020**, *2020*, 5938–5948. [CrossRef]
72. Lane, J.R.; Contreras-García, J.; Piquemal, J.P.; Miller, B.; Kjaergaard, H.G. Are Bond Critical Points Really Critical for Hydrogen Bonding? *J. Chem. Theory Comput.* **2013**, *9*, 3263–3266. [CrossRef] [PubMed]
73. Domingo, L.R.; Sáez, J.A.; Zaragozá, R.J.; Arnó, M. Understanding the Participation of Quadricyclane as Nucleophile in Polar [2σ + 2σ + 2π] Cycloadditions toward Electrophilic π Molecules. *J. Org. Chem.* **2008**, *73*, 8791–8799. [CrossRef] [PubMed]
74. Domingo, L.R.; Ríos-Gutiérrez, M.; Pérez, P. How does the global electron density transfer diminish activation energies in polar cycloaddition reactions? A Molecular Electron Density Theory study. *Tetrahedron* **2017**, *73*, 1718–1724. [CrossRef]